Modeling of implantation and mixing damage during etching of SiO2 over Si in fluorocarbon plasmas

Mingmei Wang and Mark J. Kushner

Related Articles

Additional information on J. Vac. Sci. Technol. A

Modeling of implantation and mixing damage during etching of SiO$_2$ over Si in fluorocarbon plasmas

Mingmei Wang[a)]
Department of Chemical and Biological Engineering, Iowa State University, Ames, Iowa 50010

Mark J. Kushner[b)]
Department of Electrical Engineering and Computer Science, University of Michigan, 1301 Beal Ave., Ann Arbor, Michigan 48109

Energetic ion bombardment during plasma etching of microelectronics devices is necessary to activate chemical process and define features through the ions' anisotropic trajectories. These energetic fluxes can also cause damage and mixing of the constituents of crystalline lattices. These properties are likely best modeled using molecular dynamics (MD) simulations. The computational expense of these techniques makes feature scale simulations difficult, and so motivates development of approximate methods that can be used to model full features. In this regard, an implantation and mixing model has been developed and implemented into a Monte Carlo feature profile model to simulate the mixing and damage to the underlying Si during high aspect ratio (HAR) etching of SiO$_2$ trenches. Fluxes to the surface were provided by a reactor scale model. The feature scale model was validated by comparison to the mixing produced by Ar$^+$ bombardment of Si with and without F and CF fluxes as predicted by MD simulations. Scaling of mixing damage of underlying Si during HAR of SiO$_2$ etching in Ar/C$_4$F$_8$/O$_2$ plasmas for rf bias powers of 1–4 kW was investigated. The authors found that mixing damage at the bottom of HAR features, though increasing in magnitude with increasing ion energy, does not scale as dramatically as on flat surfaces. This is due to the reflection of ions off of sidewalls which moderate the ion energies. © *2011 American Vacuum Society*.
[DOI: 10.1116/1.3626533]

I. INTRODUCTION

In plasma etching, ion-activated chemical processes preferentially etch one material with respect to another and so lead to selectivity.[1] In many etch processes, polymer layers produced by the plasma contribute to this selectivity by being less reactive on certain surfaces. A thicker polymer layer forms on those materials which then requires ions to penetrate the polymer to activate the etch of the underlying material.[2] This below-polymer etching typically requires higher energy ions. Higher energy ions also tend to be more anisotropic and so are better able to maintain critical dimensions (CD).[3] An example of this process is fluorocarbon plasma etching of trenches and vias in SiO$_2$ and stopping on a crystalline Si layer. The fluorocarbon radicals produced in the plasma deposit a polymer layer on the SiO$_2$ which is partially consumed during the etching process, thereby thinning the layer. Lack of consumption of the polymer by etching of the Si results in a thicker polymer layer on the Si.

When etching through the SiO$_2$ is nearly complete and the Si is exposed, there is often a significant over-etch period required. (The over-etch is the additional etching time required to clear the corners of the feature after the center of the feature has reached the underlying material.) At this time, selectivity of etching (that is, lack of etching of the Si)

is maintained by a C$_x$F$_y$ polymer layer of a few nanometers. The high energy ions that are required to activate etching through the overlying polymer are also capable of penetrating the polymer and damaging the underlying Si. This damage often takes the form of an amorphized mixed layer wherein the original Si atoms are both mixed with other Si atoms and with etchant or polymer atoms. High energy ions from the plasma can also implant into the Si, causing damage along their trajectory.

This damage is particularly problematic in high aspect ratio (HAR) etching of Si and SiO$_2$ in fluorocarbon plasmas.[4] To maintain the CD of these features to aspect ratios (AR) of 10–30, high energy ions (hundreds of eV to greater than 1 keV) are required. These high energy ions are more anisotropic with a narrower angular distribution, qualities required to enable reaching the bottom of the feature with sufficient energy to activate the etch. Even with their higher initial energy and narrow angular spread, the ions do suffer glancing collisions on the sidewalls of the feature. The higher the AR and the more glancing collisions that occur, the more tapered the feature tends to be, thereby requiring significant over-etching by high energy ions to clear the bottom of the feature. As the Si layer is exposed during the over-etch, ion bombardment causes mixing of etchant species (e.g., C$_x$F$_y$) into the Si and amorphizing the Si lattice.[5]

As the ion energy increases; in addition to activating etching of the material underlying the polymer and mixing the surface layers, small ions can penetrate through the passivation layer and implant into the underlying material.[6] Molecular ions tend to dissociate upon striking the surface and so

typically only atomic ions penetrate beneath the surface. (When ions come within a few angstroms of the surface, they usually neutralize through an Auger process and strike the surface as a neutral. In this paper, we will refer to the particles approaching and penetrating into the solid as ions.) Although mixing of lattice atoms with etchant species occurs only in the top few nanometers of the surface, implantation can occur deeper below the surface. In the case of Si, these implantation processes both disrupt the crystal structure and contribute to producing a mixed layer. In the case of SiO_2, the material is already amorphous and so disruption of the crystal structure is not an issue—however, formation of the mixing layer is. Optimizing these processes is then a compromise between having a high etch rate and maintaining CD with a high bias and high ion energies, and minimizing damage and mixing in the underlying material by having low ion energies.

Defect formation (e.g., vacancies, interstitials, implanted particles) in Si resulting from energetic ion bombardment (1 keV–1 MeV) has been investigated in detail in the context of etching (tens of eV $\sim$ 1 keV) and ion-implantation (several to hundreds of keV).[7–17] Characteristics of the amorphous layer produced by ions on Si surfaces have been studied in experiments[10,11] and in molecular dynamics (MD) simulations.[12–15] The sputtering yield and amorphous layer thickness have been characterized as a function of incident ion energy and angle.[16,17]

The simulation of ion implantation and mixing in crystals for ions of moderate energy ($<$ a few keV) is best addressed using MD simulations.[12–15] Although precise and first principles, MD simulations are computationally intensive. It is sometimes difficult to perform MD of etching of larger structures, such as full HAR features, rapidly enough to be compatible with computer-aided-design (CAD) tools used in industry. As such, it would be expedient to have a mechanism to address mixing and implantation in conventional feature profile models that are compatible with simulating full features and that can be incorporated into CAD tools. Such modeling techniques using Monte Carlo (MC) simulations have been discussed by Ono et al.,[18] Osano and Ono,[19] and Moroz.[20] In this regard, Shimada et al. used a level set method to simulate etching through multiple layers (e.g., polymer and mix layer, SiO_2).[21]

With this goal in mind, we have developed implantation and mixing algorithms for an MC based feature profile model. We then used the model to investigate implantation and mixing during plasma etching of HAR features through SiO_2 to an underlying Si layer in dc augmented, capacitively coupled plasmas (CCPs) sustained in $Ar/C_4F_8/O_2$ gas mixtures.[3] Results are first discussed for tailored ion fluxes incident on blank Si wafers for the purposes of validation of the model and scaling studies. We then discuss damage of underlying Si during etching of HAR trenches in SiO_2 using fluxes from the simulated CCP reactor.

The model is discussed in Sec. II. Ion energy and angular distributions (IEADs) onto the wafers from dc augmented CCPs are discussed in Sec. III. Validation of the model is described in Sec. IV, followed by a discussion of mixing of Si at the bottom of HAR features in Sec. V. Our concluding remarks are in Sec. VI.

II. DESCRIPTION OF THE MODEL

The implantation and mixing models were implemented in the Monte Carlo Feature Profile Model (MCFPM), which uses energy and angularly resolved fluxes of neutrals and ions to the substrate produced by the Hybrid Plasma Equipment Model (HPEM). The HPEM, discussed in detail in Ref. 22, will first be briefly described, followed by the MCFPM.

The HPEM is a two-dimensional model consisting of separate modules which address different physical phenomena. Each module consists of a time integration over many rf cycles, during which plasma quantities (e.g., densities and temperatures) are either recorded as a function of position and phase or recorded only as position dependent quantities averaged over the rf cycle. These values are then passed to the next module and the process iterated to a cycle-average steady state. The modules used in this study are the (1) Electron Monte Carlo Simulation for sheath accelerated secondary electrons, (2) the Fluid Kinetics Module to obtain densities, fluxes, and energies of all charged and neutral species, as well as the electric potential from the solution of Poisson's equation, and (3) the Plasma Chemistry Monte Carlo Module (PCMCM) to obtain the energy and angular distributions (EADs) of neutrals and charged species striking the wafer.

The fluxes of reactant species and their EADs from the PCMCM are then used as input to the MCFPM.[23] The MCFPM resolves the surface materials of the wafer using a two-dimensional rectilinear mesh. Each numerical cell in the mesh can represent a different solid material. Psuedoparticles representing gas phase species are directed toward the surface with velocities and angles randomly selected from the EADs produced by the HPEM. The weighting of the particle (that is, the number of atoms or molecules represented by the particle) is the same as that contained in one numerical cell in the mesh representing the solid material. The identity of the incident particle is randomly selected from the mole-fraction weighted fluxes of all species incident onto the surface. The mesh in the MCFPM is of fixed size and each mesh cell represents a different material. As such, there is not strict accounting for the different sizes of the atoms or molecules occupying each cell (e.g., Si and SiO_2). This is a weakness of the method.

When a particle strikes the surface, the particle may reflect, chemically react, adsorb, sputter, or implant. In the context of the MCFPM, an implanted particle is one that penetrates below the top surface of the solid material. The reaction that occurs is randomly chosen from a probability matrix. Since reaction probabilities typically depend on the energy and angle of incidence, for each type of incident particle the probability matrix encompasses four dimensions for (1) the solid material of the mesh cell at the site of incidence, (2) the reactions that can occur between the incident particle and the solid material at that site, (3) the energy of the incident particle, and (4) its angle with respect to the local normal of the surface. Based on the reaction chosen from this probability matrix using a sequence of random numbers, the identity of the solid mesh cell may be changed (a chemical

reaction), the solid mesh cell may be removed (an etch or sputter), or the gas phase particle may be placed on top of and join the material mesh (a deposition or adsorption). Material cells that are etched or sputtered are converted to gas phase pseudoparticles. The additional process of implantation allows for ions to penetrate below the surface.

The reaction mechanism for etching of Si and SiO$_2$ in fluorocarbon plasmas is described in detail in Refs. 23 and 24 (a full listing of the reaction mechanism is available by request from the authors). Briefly, etching of SiO$_2$ is dominantly through formation of a fluorocarbon complex by reacting with C$_x$F$_y$ radicals,
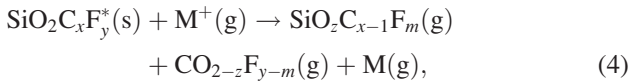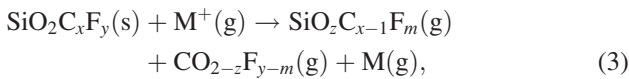
$$SiO_2(s) + C_xF_y(g) \rightarrow SiO_2C_xF_y(s), \tag{1}$$

where $x = 1$–3, $y = 1$–7.

The SiO$_2$C$_x$F$_y$ complex layer is then be activated by low energy ions (M$^+$),
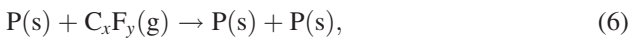
$$SiO_2C_xF_y(s) + M^+(g) \rightarrow SiO_2C_xF_y^*(s) + M(g). \tag{2}$$
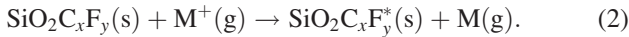
Both original and activated complex sites are etched by energetic ions (M$^+$) and produce volatile species CO$_{2-z}$F$_{y-n}$,

$$\begin{aligned} SiO_2C_xF_y(s) + M^+(g) &\rightarrow SiO_zC_{x-1}F_m(g) \\ &+ CO_{2-z}F_{y-m}(g) + M(g), \end{aligned} \tag{3}$$

$$\begin{aligned} SiO_2C_xF_y^*(s) + M^+(g) &\rightarrow SiO_zC_{x-1}F_m(g) \\ &+ CO_{2-z}F_{y-m}(g) + M(g), \end{aligned} \tag{4}$$

where $x = 1$–3, $y = 1$–7, $z = 0$–2, $m = 0$–7, and M is a neutral corresponding to ion M$^+$.

C$_x$F$_y$ neutrals deposit a polymer layer (P) on the complex surface. Further deposition by C$_x$F$_y$ radicals produces a thicker polymer layer. The polymer layer is etched by F radicals to produce CF$_x$ gas,

$$SiO_2C_xF_y^*(s) + C_xF_y(g) \rightarrow SiO_2C_xF_y(s) + P(s), \tag{5}$$

$$P(s) + C_xF_y(g) \rightarrow P(s) + P(s), \tag{6}$$

$$P(s) + F(g) \rightarrow CF_x(g). \tag{7}$$

The remaining Si is etched dominantly by F atoms diffusing through the polymer layer, passivating the Si,

$$SiF_{n-1}(s) + F(g) \rightarrow SiF_n(s), \tag{8}$$

$$SiF_3(s) + F(g) \rightarrow SiF_4(g), \tag{9}$$
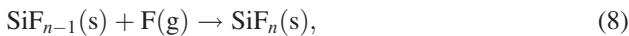
where $n = 0$–4.

The primary differences between the mechanism we used in this paper and that described in Refs. 23 and 24 are additional reactions of oxygen radicals with the polymer layer [Eq. (10)] and direct sputtering of Si and SiF$_n$ [Eq. (11)],

$$P(s) + O(g) \rightarrow CO_zF_y(g), \tag{10}$$

$$SiF_n(s) + M^+(g) \rightarrow SiF_n(g) + M(g), \tag{11}$$
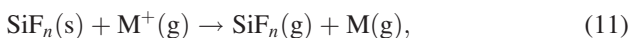
where $z = 0$–2, $y = 0$–2, $n = 0$–3. The oxygen radicals are produced by electron impact dissociation of O$_2$ and control

the thickness of the polymer layer through oxidizing reactions.

In HAR etching, ions undergo glancing collisions on the sidewalls. In addition to neutralizing in these collisions and proceeding as a hot neutral, there is also a loss of energy. In the model, we use an angle dependent loss of energy for such ions. The algorithm for energy loss as a function of angle is described in Ref. 24. Briefly, grazing ions (defined as having an angle of incidence approaching $90°$ with respect the local surface normal) retain 85% of their incident energy and reflect specularly. As the angle of incidence decreases to $60°$, the retained energy decreases linearly toward thermal, and the reflection angle transitions from specular to diffuse. The same algorithm is applied to hot neutrals.

Although both monoatomic and polyatomic ions are incident onto the surface, for the purposes of the implantation model, we assumed that large polyatomic ions dissociate on impact and monoatomic fragments continue into the surface. In the context of fluorocarbon etching in Ar/C$_4$F$_8$/O$_2$ gas mixtures, the ions we allowed to penetrate into the surface are Ar$^+$, F$^+$, Si$^+$, C$^+$, and O$^+$. We included the same algorithms for the hot atom counterparts of these ions. The energy and angle of incidence of the atomic ions (or hot atoms) determine the distance of penetration and deposition of energy into the lattice. The energy deposition along the slowing down path results in dislocations and mixing of the crystal. The slowed ions implant into the lattice, displacing atoms which produce additional mixing. Nonreactive interstitially implanted ions, such as Ar, then diffuse through the crystal, eventually returning to the plasma.

These algorithms were incorporated into the MCFPM to track the trajectory of implanting particles and to simulate mixing during implantation. The algorithms are schematically shown in Fig. 1. The average stopping range that particles travel in materials (for these simulations, photoresist, SiO$_2$, polymer, and Si), λ, was estimated using Stopping and Ranges of Ions in Matter (SRIM) as a function of energy.[25] SRIM was originally developed to address implantation and sputtering for energy ranges of many keV/amu or greater. We are using SRIM over a lower energy range and acknowledge that there is some degree of approximation in doing so. To approximate photoresist (PR), we used PMMA (polymethylmethacrylate) and to approximate fluorocarbon polymer, we used PTFE (polytetrafluorethylene or Teflon). When a particle strikes the wafer surface, a random number $r = (0,1)$ is used to determine its theoretical penetration distance into the material,

$$\lambda = -\bar{\lambda} \ln(1 - r). \tag{12}$$

(Note that for each expression that requires a random number, a different random number generator is used.) Based on the particle's current position, the physical distance that the particle needs to travel along its trajectory through the current mesh cell to reach the next mesh cell is computed, λ_a (see Fig. 1). If $\lambda_a < \lambda$ then the particle is assumed to continue on its trajectory. During its transition along the initial path, the particle loses an amount of energy for initial energy ϵ_{in},
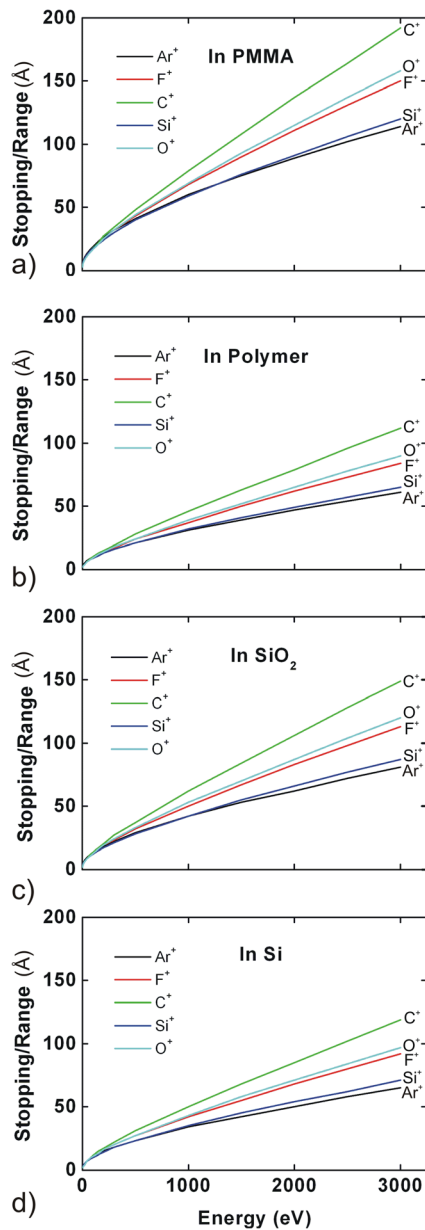
FIG. 1. (Color online) Schematic of the algorithm for implanting and mixing incorporated in the Monte Carlo Feature Profile Model. (N* is an empirically derived number dependent incident energy that defines the maximum number of mixing steps.) The length λa is the distance traveled within a cell that the probability of collisions is based on.

$$\Delta\varepsilon = \varepsilon_{in}(1 - \exp(-\lambda_a/\lambda)). \tag{13}$$

If $\Delta\varepsilon/\varepsilon_{in} > r$, where $0 < r < 1$ is a random number, then the amount of energy deposited along the path may produce lattice dislocations. Otherwise, atoms simply oscillate in the same lattice location after absorbing $\Delta\varepsilon$. The dislocation depends not only on the energy absorbed but also on steric hindrance. When a lattice dislocation occurs, the identity of adjacent numerical mesh cells is exchanged to denote formation of a dislocation—or a mixing event. If the region of the mesh is totally one material, this exchange will not produce a stoichiometric defect, but will produce a structural defect. If the local environment is heterogeneous (that is, near a boundary between materials), the mixing exchange will blur the boundary.

When the particle enters the next cell, we return to the first step [Eq. (12)], and repeat the process with a reduced particle energy $\varepsilon_{in} = \varepsilon_{in} - \Delta\varepsilon$. If $\lambda_a > \lambda$, we deem that the particle has stopped and implanted. Before implanting the particle, the adjacent cells are randomly moved to evacuate the implantation site, thereby constituting additional mixing. The cell occupying the implantation site is randomly moved to a neighboring site, freeing up the original site into which the implanted atom is placed. The cell that occupied the site now occupied by the first displaced cell is then moved in a random direction to displace another cell. The successive displacement of cells continues until a cell is pushed above the material surface to the gas interface or the number of displacement steps exceeds a maximum value based on the incident energy of the ion. The number of steps was determined by $n = \varepsilon_{in}/2$ by comparison to experiments,

where ε_{in} is expressed in eV. This number of steps is based on the energy of the particle when first striking the surface.

In our model, energetic ion bombardment of hydrocarbon PR can lead to chain scission of the polymer backbone (degradation) followed by cross-linking (gelling) of adjacent dangling bonds. This cross-linking produces a hardened material that is more resistive to sputtering and etching. For example, the hardness of PMMA significantly increases upon high energy ion bombardment due to this scission–cross-linking process.[26] The etch rate of PMMA in Ar plasmas initially decreases and then is constant, presumably due to a saturation of the cross linking in the near surface layers.[27]

To account for these processes, we included bond breaking in the PR and conversion to cross-linked sites. The sputtering yield of the cross-linked PR sites is 5 times smaller than that of normal sites. Bond breaking in the PR is accounted for by ion impact, which results in either sputtering or in transferring more than the bond energy to the PR. These impacts produce free-radical sites having dangling bonds. Assuming a hydrocarbon polymer, bond breaking by either sputtering an H or C atom, or scissioning the polymer backbone, will create a free-radical site on a C atom. Cross-linking (the bonding of two adjacent polymer chains) then results from reactions between two free-radical sites.

III. IEADS ONTO THE WAFER

In Ar/C$_4$F$_8$/O$_2$ plasmas, the dominant small ions (and their hot atom counterparts) are Ar$^+$, F$^+$, C$^+$, Si$^+$, and O$^+$. The stopping ranges of these particles in PMMA/PR, PTFE/polymer, Si, and SiO$_2$ were calculated using SRIM and are shown in Fig. 2 as a function of the incident particle energy. The penetration depth increases proportionally with ion energy. For a given energy, the penetration distances for materials rank, long to short: PR > SiO$_2$ > Si > polymer. For ions in the same material, the ranking of penetration depth is C$^+$ > O$^+$ > F$^+$ > Si$^+$ > Ar$^+$. The penetration depths range up to 200 Å at 3000 eV, which covers the expected range of ion energies incident onto the wafer in our plasmas.

Ar/C$_4$F$_8$/O$_2$ plasmas were simulated in a dc augmented CCP reactor with the HPEM using the same geometry as in Ref. 3. The base case operating conditions are Ar/C$_4$F$_8$/O$_2$ = 80/15/5 at 40 mTorr with a flow rate of 300 SCCM (standard cubic centimeters per minute at standard temperature and pressure). The substrate is biased at 10 MHz delivering a power of 4 kW and the dc electrode delivers 200 W.

From the PCMCM we obtained IEADs for Ar$^+$, F$^+$, and O$^+$ as shown in Fig. 3 as a function of rf bias power. The ion fluxes at the center of the substrate are shown in Fig. 4. The rf amplitudes V_{rf} and dc biases V_{dc} for these cases are as follows: 1 kW ($V_{rf} = -617$ V, $V_{dc} = -114$ V), 2 kW ($V_{rf} = -894$ V, $V_{dc} = -155$ V), 3 kW ($V_{rf} = -1215$ V, $V_{dc} = -203$ V), and 4 kW ($V_{rf} = -1500$ V, $V_{dc} = -229$ V). The power is specified in the model and the rf voltage is adjusted to obtain this power. Although C$^+$ and Si$^+$ are included in the model, they will not be discussed further here due to their low fluxes onto the surface (smaller by a factor of 10^3–10^5 compared to the major ions). The peak energies of the ions increase nearly

FIG. 2. (Color online) Stopping range as a function of ion energy calculated from SRIM for Ar^+, F^+, O^+, Si^+, and C^+ in (a) PMMA, (b) C_xF_y polymer (Teflon), (c) SiO_2, and (d) Si.
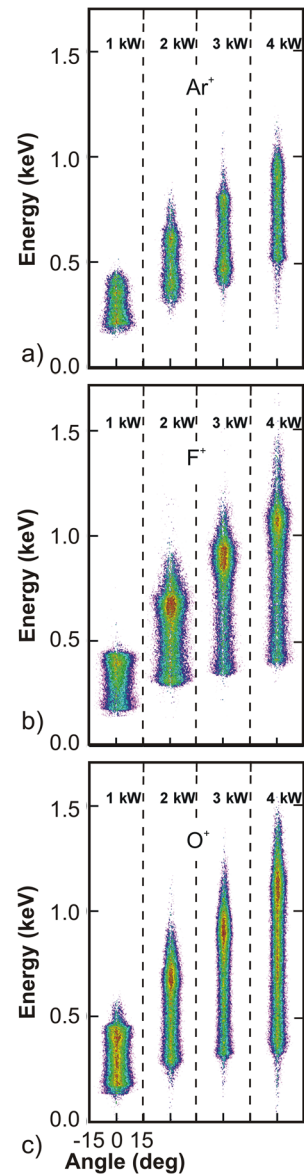

FIG. 3. (Color online) Energy and angular distributions of ions onto the wafer surface at rf bias powers of 1–4 kW for (a) Ar^+, (b) F^+, and (c) O^+. The operating conditions are $Ar/C_4F_8/O_2 = 80/15/5$ at 40 mTorr with a flow rate of 300 SCCM. The substrate is biased at 10 MHz and the dc electrode delivers 200 W.

linearly with increasing rf bias power for all particles. The heavier ions have narrower angular spreads, consistent with their longer crossing times across the sheaths.[28] At higher bias power, the IEADs are narrower in angle due to the stronger sheath electric fields orienting the ions more toward the vertical.

IV. VALIDATION OF THE MODEL

For purposes of validation, Ar^+ bombardment of Si was modeled using a mesh resolution of 3 Å with each mesh cell approximately representing 1 atom. Profiles are shown in Fig. 5 after 30 s with an ion flux of 7×10^{14} cm^2 s^{-1} at normal incidence for ion energies of 20, 50, 100, and 200 eV. (For the purpose of better observing the mixing in bulk Si,

FIG. 4. (Color online) Ion fluxes onto the wafer surface at rf bias powers 1–4 kW ($Ar/C_4F_8/O_2 = 80/15/5$, 40 mTorr, 300 SCCM, 10 MHz).

JVST A - Vacuum, Surfaces, and Films

FIG. 5. (Color) Implanting and mixing depth in Si substrate under Ar$^+$ bombardment with an energy of (a) 20 eV, (b) 50 eV, (c) 100 eV, and (d) 200 eV. The Si is shown multilayer (different colors) to better display the mixing. The green is interstitial argon.
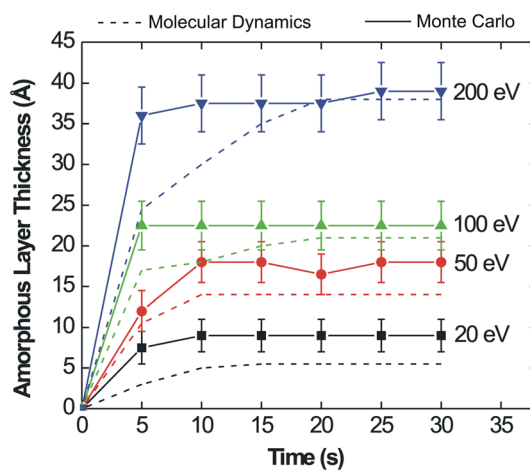

FIG. 6. (Color online) Amorphous (mixing) layer depth as a function of ion energy. Solid lines are results from the model, dashed lines are published MD simulations from Ref. 13. The mixing layer forms quickly before achieving a near steady state.

is 1–2 Å at 20 eV and increases to 6 Å at 200 eV. We also reproduce the rapid onset of mixing damage (a few seconds) before reaching a steady state, though we reach that steady state sooner than the MD simulations. The thickness of the mixing layers is close to the ranges calculated from SRIM, though it sometimes exceeds these ranges. The ranges are average values from a statistical distribution of stopping distances, and so there are significant numbers of individual particles whose penetration distances are greater than the ensemble average. We see this effect in the model, individual particles penetrating deep into the material, and the end result is that mixing and damage occur at depths beyond the ensemble averaged stopping distance.

V. SCALING OF IMPLANTATION AND MIXING

In order to investigate the degree of implantation and mixing under etching conditions in an Ar/C_4F_8/O_2 CCP, a multilayer Si structure was used similar to that described earlier for comparisons with the MD simulations. The top layer is SiO_2 of thickness 9 nm followed by alternating monolayers of Si (3 Å). A thin SiO_2 layer was chosen to represent an actual etch process at the time that SiO_2 is thinned as the Si layer is approached. The fluxes of radicals and ions incident onto the surface are listed in Table I. The fluxes are obtained from the rf 4 kW case ($V_{rf} = -1500$ V, $V_{dc} = -229$ V). We first artificially constrained the ion energies to be monoenergetic from 1 to 1000 eV but having the same magnitude of fluxes as obtained from the simulation in order to observe general scaling trends.

The resulting etch profiles after processing for 25 s are shown in Fig. 7. At energies of 1 eV, which are lower than the threshold energy for etching and implanting, only polymer deposition (brown squares) occurs on the surface. When the ion energy is increased to 10 eV, which is marginally higher than the threshold energy for sputtering of C_xF_y polymers and implanting while still lower than that of most etching reactions, sputtering of polymer occurs. This produces

the initial distribution of atoms was color coded red and dark blue in alternating layers, but otherwise they represent the same material. Green squares represent implanted Ar particles.) These energies were chosen to enable comparison with the MD simulation of Humbird et al.[13] The flux and duration of bombardment of Ar$^+$ corresponds to 30 monolayers of Ar$^+$ fluence. Charging effects were not included to better compare the mixing under the same conditions as the MD simulations. The depth of the mixing layer in the simulation is determined by the maximum depth for which there is significant disturbance of the lattice. That is, a single errant particle deeply penetrating will not constitute the mixing depth.

At 20 eV, ions penetrate only a few monolayers of Si and little mixing occurs. As the ion energy increases, ions penetrate deeper into the bulk Si and induce more mixing during and after implantation. The amorphous layer thickness as a function of bombardment time is shown in Fig. 6. The final mixing layer thickness is about 9 Å at 20 eV to 38 Å at 200 eV, generally in good agreement with the MD simulation (dashed lines), especially at higher ion energy (e.g., 200 eV). The statistical variation in the thickness of the mixing layer

TABLE I. Fluxes of radicals and ions incident onto the wafer.

Particle	Flux (10^{15} cm^{-2} s^{-1})	Particle	Flux (10^{15} cm^{-2} s^{-1})
Ar^+	4.23	CF	0.32
CF_3^+	0.26	CF_2	1.86
CF_2^+	0.15	C_2F_4	29.6
F^+	0.08	C_3F_5	0.32
O^+	0.04	F	3.2
$C_2F_4^+$	4.28	F_2	0.04
$C_3F_5^+$	1.23		
$C_3F_6^+$	0.002		
$C_4F_7^+$	0.006		
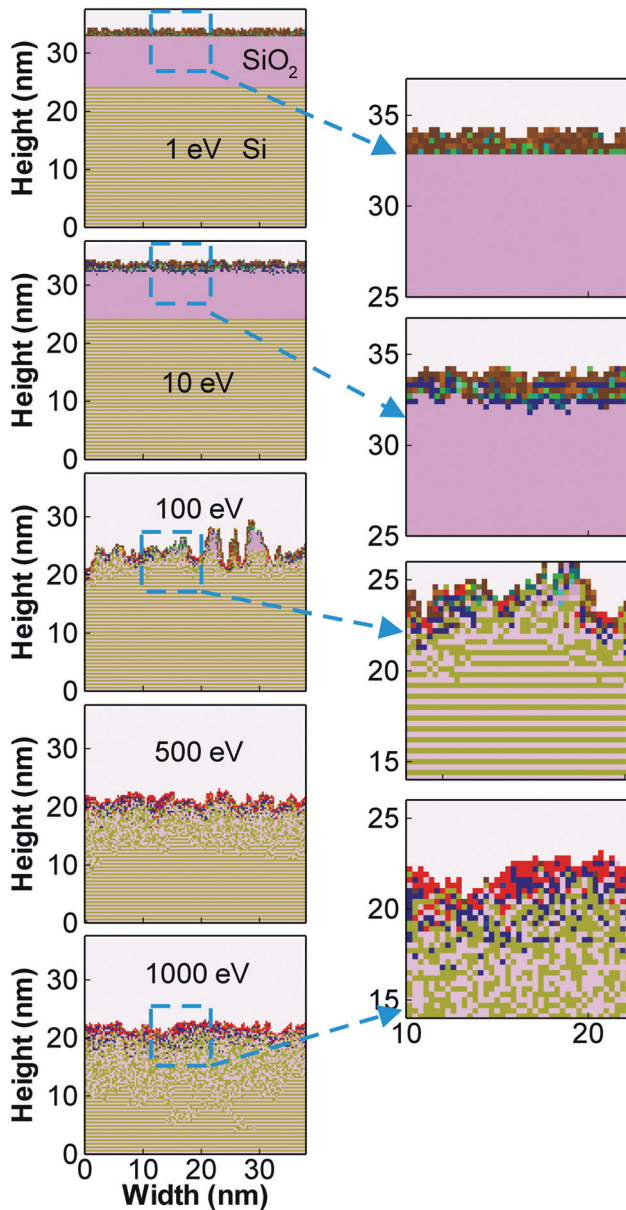
FIG. 7. (Color) Profile and composition during etch of SiO$_2$ over Si at ion energies of (top to bottom) 1, 10, 100, 500, and 1000 eV. Although the ion energies are fixed, the composition of the fluxes is as produced by the reactor scale model. The Si is shown multilayered to better visualize mixing. Color coding: Brown and green—polymer species. Dark blue—implanted particles. Red—sputtered residues.

polymer segments (red) and implanted species (dark blue) on the top of the SiO$_2$ but there is essentially no etching. At 100 eV, sputtering and etching reactions dominate. More broken polymer segments (red) are on the surface, to a depth of about 1 nm. Mixing also begins to appear as a result of implantation to a depth of about 2 nm. The surface significantly roughens as micromasking due to random collections of thicker polymer block ions. The SiO$_2$ is virtually gone at sites that are not micromasked, with the top layer becoming a mixture of polymer and Si.

Although micromasking resulting in significant roughening is an experimentally observed effect,[29,30] its representation here may be exaggerated due to the discreteness of the Monte Carlo mesh. Polymer deposition on any given site occurs strictly in the vertical direction, as opposed to having a lateral component to the deposition, an effect that is better represented in MD simulations.[13] Although the average polymer layer thickness is well represented in the MC simulation, its roughness is exaggerated due to the need to "stack cells," which then exaggerates micromasking.

As the ion energies increase to 500 eV and above, deeper implantation occurs with a higher degree of mixing, and etching of Si commences. The polymer rich mixing layer at 1000 eV is about 5 nm, while the total mixing layer below the polymer rich layer is about 12 nm thick. At the higher ion energies, Si sputtering and etching also occurs through the thick polymer layer.

Implantation and mixing as a function of rf bias power (1–4 kW) using the actual ion energy distributions and the same test structure as used previously are shown in Fig. 8 after etching for 5 s. Etching profiles at the same etch depth for these bias powers are shown in Fig. 9. Two cases are shown—with a finite thickness of SiO$_2$ as might occur as the etch approaches the Si layer and approximately when the Si interface is reached. As with the monoenergetic ions, the etch proceeds through the top SiO$_2$ layer and nearly terminates on the underlying Si layer. There is an initial rapid etch through the SiO$_2$ followed by a slow etch into the Si. Note that there is roughness produced by micromasking resulting from regions having statistically larger polymer thickness, as discussed previously. As the rf power and ion energies increase, there is more mixing of the underlying Si layers below the etched surface. For a constant etch depth, the higher biases statistically have ions which have long ranges through the SiO$_2$ and which penetrate into the Si. For example, at and above 4 kW, ions penetrate through the remaining SiO$_2$ and produce mixing in the underlying Si to a depth of 5–8 nm even before the etch has reached the Si interface. At a bias of 1 kW, there is negligible penetration of ions through the remaining SiO$_2$. When the etch reaches the Si interface, the mixing depth is 10–12 nm at 4 kW, whereas at 2 kW the depth of mixing is 6 nm. At this point, there is significant mixing even for the 1 kW case.

Even though the peak ion energies scale with bias power, at all bias powers there is a distribution of ion energies, as shown in Fig. 3. There is clearly more ion penetration and mixing at the higher bias powers due to the higher range of
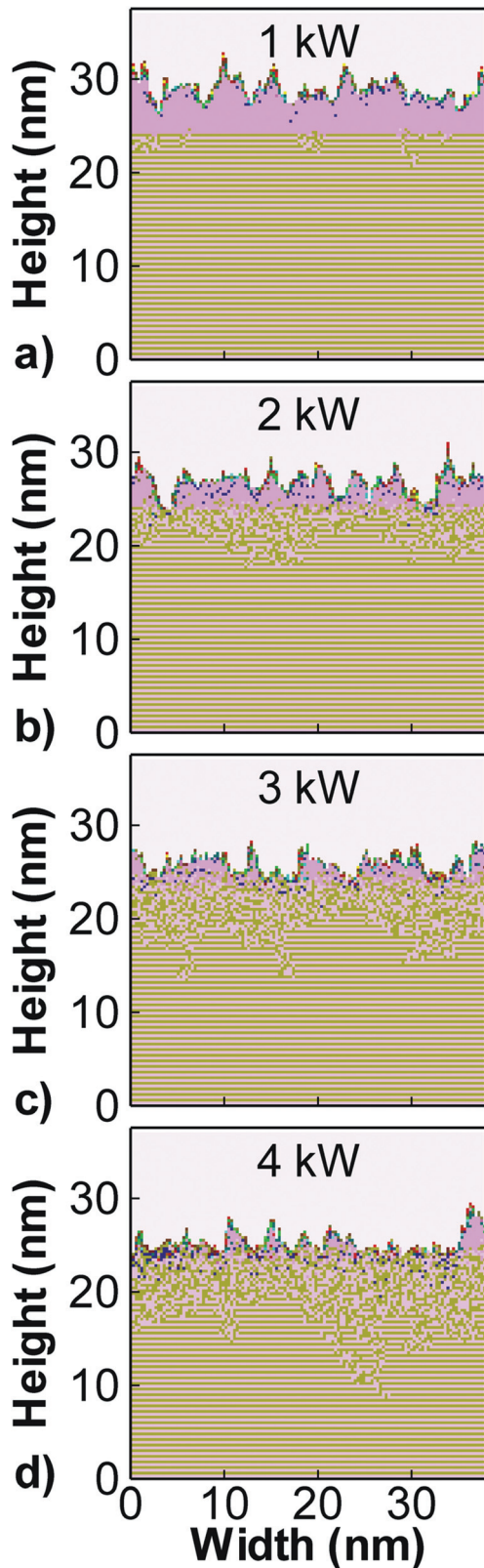
FIG. 8. (Color) Profile and composition during etch of SiO_2 over Si for a constant etch time of 5 s for rf powers of (a) 1 kW, (b) 2 kW, (c) 3 kW; and (d) 4 kW. The color coding is the same as for Fig. 7 The mixing depth increases due to the thinning of the SiO_2 layer and longer range with increasing power.

ion energies. At the same time, a polymer layer persists due to the low energy portion of the ion distribution.

As HAR trenches are etched through SiO_2 to a Si layer below, tapering of the feature results in Si at the center of the feature being exposed to the plasma prior to the sides of the feature. An over-etch is therefore required to clear the feature, which affords greater opportunity for damage to the Si to occur. Mixing of Si at the bottom of HAR trenches etched through SiO_2 was investigated as a function of rf bias power. For example, trenches having an aspect ratio of 15 are shown in Fig. 10. Profiles are shown for the same etching time 59 s, for bias powers of 1–4 kW. The bottoms of the features are also shown with over-etching for the different etch times required to clear the bottom of the feature. For comparison of etch selectivity, an etch profile is shown in the absence of implantation mixing or cross-linking at 4 kW after etching for 28 s with a similar etch depth of PR. Implantation and mixing in the Si through the overlying polymer layer produces an amorphous, mixed layer at the bottom of the feature. The higher biases produce more mixing though not to the degree predicted in Fig. 8 for a flat surface. The initially larger ion energies are moderated by glancing collisions with the sidewalls, thereby reducing their energy by the time they reach
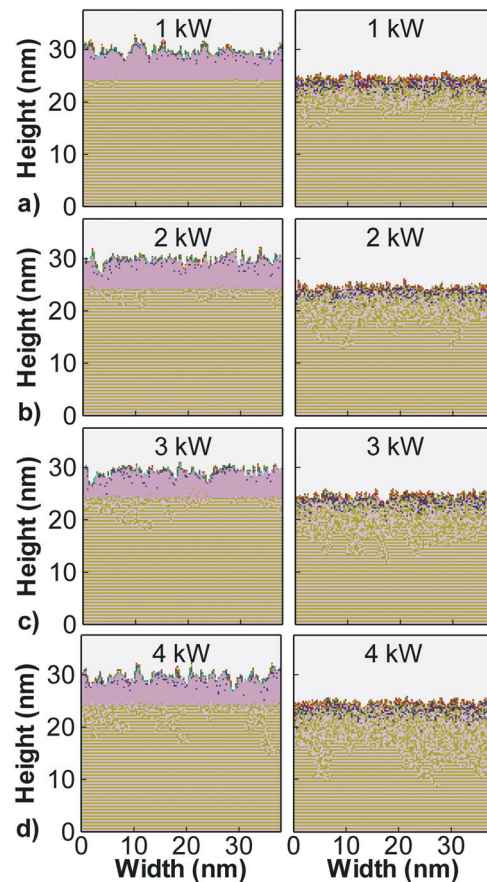

FIG. 9. (Color) Profile and composition during etch of SiO_2 over Si for a constant etch depth for rf powers of (a) 1 kW; (b) 2 kW; (c) 3 kW; and (d) 4 kW. (Left) With a finite thickness of SiO_2 and (right) approximately when the Si interface is reached. The color coding is the same as for Fig. 7. At higher powers, mixing in the Si occurs even with a thick SiO_2 layer due to the longer range of ions.

the bottom of the feature. As long as these ions have energies exceeding the etching threshold, the feature is cleared. However, the range of these lower energy ions into the underlying material is significantly reduced.

Ion interactions with hydrocarbon PR produce dangling bonds which then cross-link—and the cross-linked polymer surface is then more resistive to etching. As such, there is less degradation of the PR with increasing bias as the PR becomes more resistive through the cross-linking. This enables the CD to be maintained to higher aspect ratios. Although not the focus of this study, the cross-linked polymer is shown in Fig. 10 as the darkened layer on top of the PR.

Higher bias powers are usually preferred in HAR etching since the etch rate is higher, the feature is straighter, and charging effects are minimized due to the higher ion energies and narrower angular distributions. There are, however, drawbacks to etching with higher ion energies. As shown in Fig. 10, higher energy ions cause deeper implantation and more mixing in the underlying Si at the moment that SiO_2 is etched through. To investigate the scaling of mixing depth as a function of rf bias power and over-etch time, we simulated etching of a trench with an aspect ratio of 1 (trench width = trench depth ≈ 25 nm) as shown in Fig. 11(a). The underlying Si layer is a multilayer structure with two colors representing the same material to better visualize the mixing. The mesh resolution is 3 Å. Over-etching begins when the SiO_2 is removed from the middle of the trench. The depth of the mixing layer generally increases with over-etch time to an asymptotic value, which increases with increasing bias power. The time evolution of the mixing depth at different rf bias powers is shown in Fig. 11(b). The average mixing depth is plotted using results from ten identical profiles simulated with different random seed numbers. The onset of mixing during over-etch is somewhat randomly distributed and does not have a clear scaling correlation with rf bias

power. This is because the first implanted particles are not necessarily more energetic at higher rf bias power since there is a distribution of ion energies which extends to lower energies. The general trend is an increase in mixing depth with increasing rf power up to about 15 nm at 4 kW.

Note that in these cases, there is significant micromasking of the SiO_2, which produces large variations in the height of the bottom of the trench.[29,30] As mentioned previously, its representation here may be exaggerated due to the numerical meshing of our model. Micromasking is also expected to worsen (on a relative basis) as the feature size decreases. Although particle (ions and neutrals) fluxes can be quite uniform along the wafer surface at macroscale, they can be statistically nonuniform on a microscale surface. For our conditions, the ion flux is as high as 10^{16} cm^{-2} s^{-1} and neutral flux is as high as 10^{17} cm^{-2} s^{-1}. The time interval between two incident ions on a single surface site (3 Å × 3 Å) is around 0.1 and 0.01 s between two incoming neutrals, an effect that is exacerbated by shadowing in high
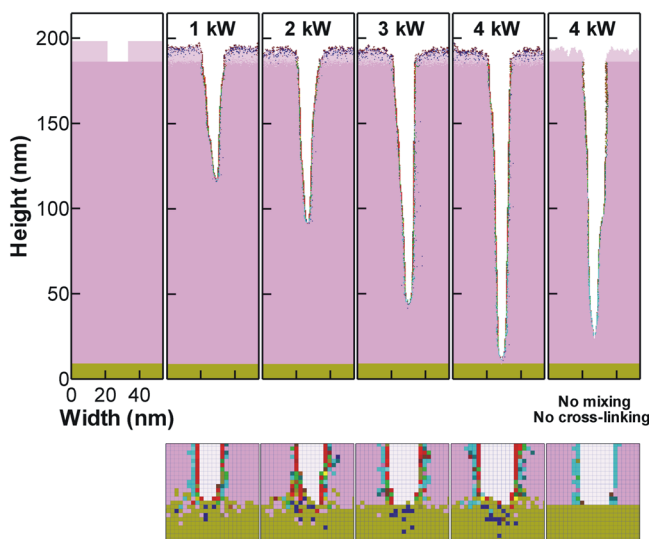

FIG. 10. (Color online) Etch properties as a function of bias power (1–4 kW). (Top row) Etch profiles as a function of power for the same etch times. (Bottom row) Mixing at the bottom of the trench for the same over-etch time. A case without implantation and PR cross-linking is shown for comparison.
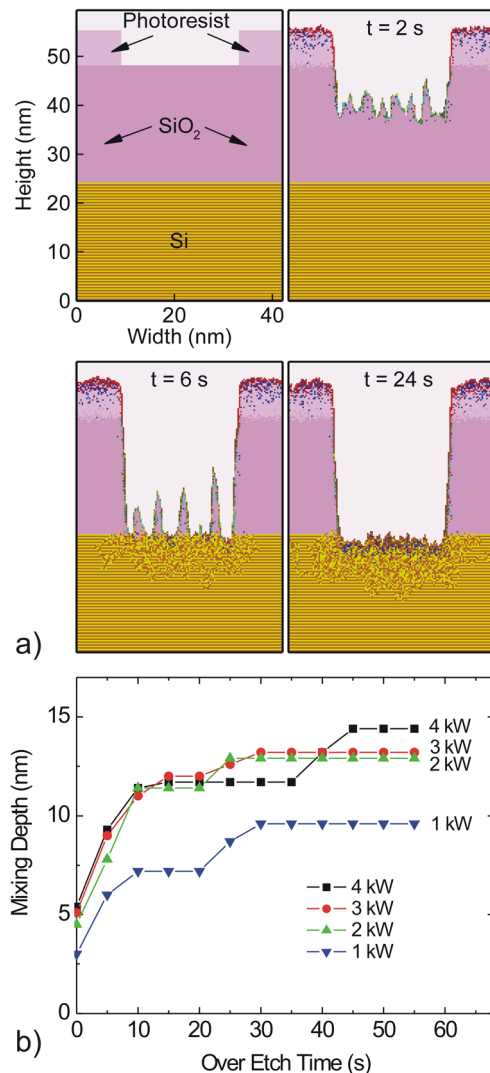

FIG. 11. (Color online) Mixing layer depth as a function of over-etch time. (a) Etching of a small AR feature as a function of time. (b) Mixing layer depth in this feature as a function of over-etch time for bias powers of 1–4 kW.
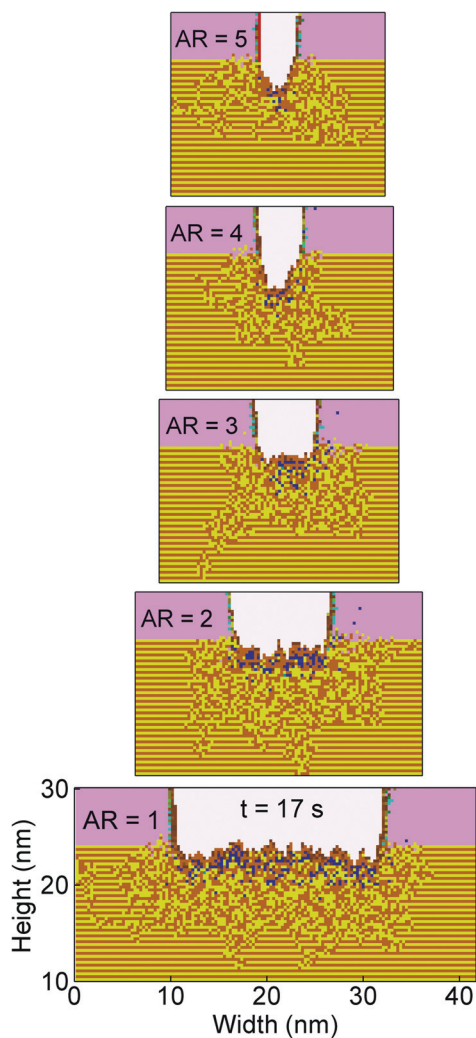
FIG. 12. (Color) Etching profile and mixing layer shape as a function of feature aspect ratio (from top to bottom, 5, 4, 3, 2, and 1) for a bias power of 4 kW. At high AR, the relative lateral extent of the mixing layer is larger.

FIG. 13. (Color) MCFPM simulation of polymer deposition and mixing in underlying Si for fluxes of (a) $CF/Ar^+ = 99/1$. The CF is at 300 K and the Ar^+ is monoenergetic at 200 eV. (b) $CF/F/Ar^+ = 20/5/1$. The CF is at 1.5 eV, the F at 300 K, and the Ar^+ is at 200 eV. The enlarged images are for (middle) as etched with Ar implantation (dark blue) and (bottom) post-etch with Ar having diffused out of the mixing layer.

aspect ratio features having small openings to the plasma. Statistically, it is likely to have a sequence of radicals into the feature that locally produces a thicker polymer layer and other locations have an anomalously thin polymer layer. The end result is severe micromasking that produces needlelike structures that requires an over-etch to be removed. Fortunately, the selectivity is high enough that the needles can be removed without significant damage to the underlying Si. The micromasking is amplified compared to previous cases (as in Figs. 7–9) due to the thicker SiO_2 layer and longer processing time. This micromasking is also more apparent in this lower aspect ratio feature compared to HAR features, as in Fig. 10, In HAR features, micromasking is remediated by ions reflected from the sidewalls.

AR is another factor that may affect the mixing depth and shape of the damaged layer. For example, profiles for the bottom of trenches having different aspect ratios are shown in Fig. 12 for etching with an rf bias of 4 kW. The feature depth is 25 nm for an etch time of 17 s. The mesh resolution is 3 Å. For an AR = 1, the trench bottom is relatively flat as is the underlying implanting and mixing layer. Some micro-
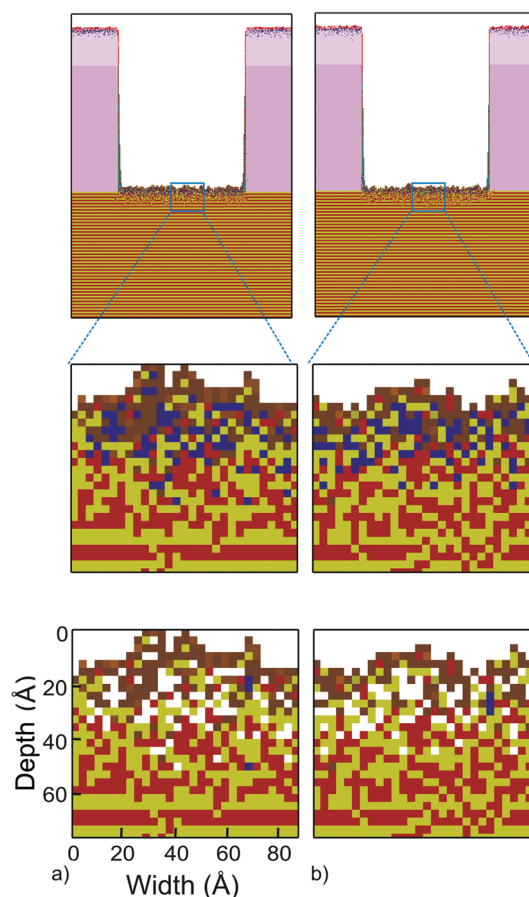
trenching appears near the sidewalls. The thickness of the mixing layer (around 14 nm) does not appreciably change with AR nor does the range of the mixing layer extending laterally to the sides of the feature (around 5 nm) appreciably change.

However, as the AR increases by having a narrower feature while the lateral range of mixing remains constant, the relative extent of the mixing increases—that is, the lateral extent of mixing compared to the width of the feature increases. The more tapered profile at higher AR also results in more ions striking a surface at a more normal angle of incidence near the corners of the trench. The range of the ions into the solid at near normal incidence is generally larger than at grazing incidence. Therefore, even though on average the ion energy is lower at the bottom of HAR features due to sidewall collisions, the mixing layer retains a broad extent.

Another consequence of mixing is vertical spatial variation in the mole fractions of species. For example, Si has a mole fraction of 1.0 in the undisturbed lattice below the mixing layer and a lower value in the mixing layer where there are, in these cases, significant mole fractions of C_xF_y. Predicted mixing layers on flat surfaces of trench bottoms are
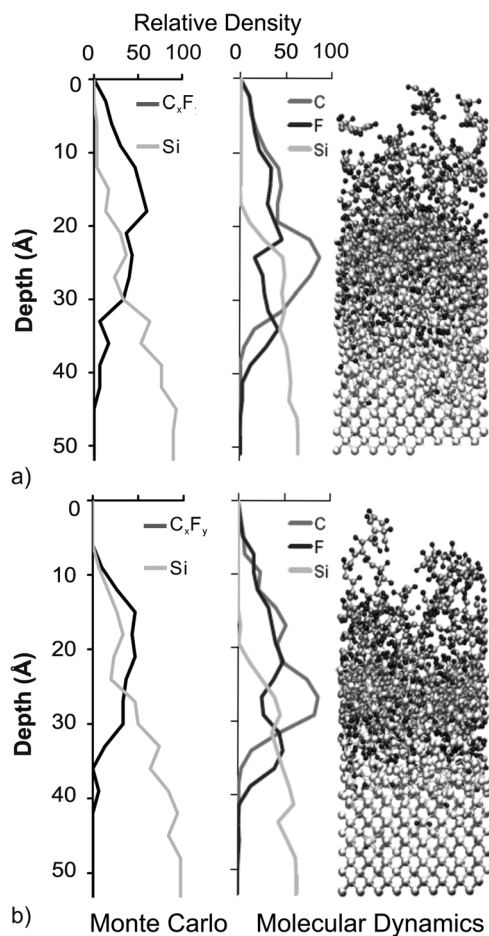
FIG. 14. Comparison between (left) MCFPM and (right) molecular dynamics simulation (from Ref. 31) for atomic or molecular constituents as a function of depth for fluxes of (a) CF/Ar$^+$ = 99/1. The CF is at 300 K and the Ar$^+$ is monoenergetic at 200 eV. (b) CF/F/Ar$^+$ = 20/5/1. The CF is at 1.5 eV, the F at 300 K, and the Ar$^+$ is at 200 eV. The Monte Carlo results are "post-etch" with the implanted Ar atoms removed.

shown in Fig. 13 after 8 s with parameters chosen to compare to the MD simulations of Végh et al.[31] Mixing of a Si layer was simulated for incident fluxes of CF/Ar$^+$ = 99/1 with the CF at 300 K and the Ar$^+$ at 200 eV [Fig. 13(a)]; and for fluxes of CF/F/Ar$^+$ = 20/5/1, with CF at 1.5 eV, F at 300 K, and Ar$^+$ at 200 eV [Fig. 13(b)]. The Ar$^+$ flux is 10^{15} cm^{-2} s^{-1}. Results are shown "as etched" with the Ar still implanted, and "post-etch" after the Ar has diffused out of the mixed layer. The post-etch feature was obtained by simply removing the Ar from the lattice, assuming that the interstitial Ar would diffuse out during subsequent heating of the wafer without significantly disturbing the atom arrangement. There are some remaining dark blue squares, which are SiO$_2$C$_x$F$_y$ complex.

For both cases the mixing layer has a reached steady state with little additional change in composition with time. The thickness of the polymer layer on top of Si will; however, continue to grow since there is almost no etching for the CF/Ar$^+$ case and very slow etching for the CF/F/Ar$^+$ case. In our model, the mixing depth under the C$_x$F$_y$ polymer for either case is around 20–40 Å, which is comparable to the MD results.[31] A comparison of our computed mixing layer

composition as a function of depth with the MD simulation is shown in Fig. 14. The fluxes onto the surface in the MCFPM are the same as in the MD simulations. We do not resolve individual C and F atoms on the surface, and so our comparison for surface composition is based on polymer cells, referred to as C$_x$F$_y$. A difference between the accounting between our results and the MD is that C$_x$F$_y$ polymer molecules are counted in our model whereas C atoms and F atoms are separately counted in the MD simulation. For the CF/Ar$^+$ case [Fig. 14(a)], the mixing layer in our model starts from about 13 Å and ends at about 42 Å, which is comparable to MD result (18–41 Å). For the CF/F/Ar$^+$ case [Fig. 14(b)], although the mixing layer in our model is from 8 to 35 Å which is a bit shallower than MD result (20–41 Å), the thickness of the mixing layer is still comparable. In both cases, there is a region about 10 Å thick where the C/Si ratio is about 1.

VI. CONCLUDING REMARKS

Implantation and mixing have been incorporated into a Monte Carlo based feature profile model to predict damage during HAR etching of SiO$_2$ over Si in Ar/C$_4$F$_8$/O$_2$ plasmas. A quantitative validation of the model was conducted for mixing of an Si substrate during Ar$^+$ bombardment by comparison with MD simulations. When increasing either bias power or ion energy, particles implant deeper and induce more mixing in the underlying material. For sufficiently thin SiO$_2$ layers over Si, the particles are able to penetrate through the SiO$_2$ to produce mixing in the underlying Si. Although the onset of mixing during over-etch has a somewhat statistical distribution, the mixing depth is proportional to bias power at the steady state. As the AR increases, the relative extent of the mixing layer laterally beyond the feature increases. For low AR, the bottom of the etch profile is relatively flat as is the mixing layer with small amounts of microtrenching near the sidewalls. As the AR increases and feature width shrinks, the bottom of the profile is more tapered, whereas the lateral extent of the mixing is nearly constant. On average, mixing is deeper at lower AR due to there being more energetic ions incident onto the bottom of the feature —more ions strike the bottom prior to having glancing sidewall collisions.

ACKNOWLEDGMENTS

[1]K. H. R. Kirmse, A. E. Wendt, S. B. Disch, J. Z. Wu, I. C. Abraham, J. A. Meyer, R. A. Breun, and R. C. Woods, J. Vac. Sci. Technol. B 14, 710 (1996).
[2]G. S. Oehrlein and H. L. Williams, J. Appl. Phys. 62, 662 (1987).
[3]M. Wang and M. Kushner, J. Appl. Phys. 107, 023309 (2010).
[4]S. Noda, N. Ozawa, T. Kinoshita, H. Tsuboi, K. Kawashima, Y. Hikosaka, K. Kinoshita, and M. Sekine, Thin Solid Films 374, 181 (2000).
[5]D. Humbird and D. B. Graves, J. Appl. Phys. 96, 65 (2004).
[6]S. Rauf, T. Sparks, P. L. G. Ventzek, V. V. Smirnov, A. V. Stengach, K. G. Gaynullin, and V. A. Pavlovsky, J. Appl. Phys. 101, 033308 (2007).
[7]I. H. Wilson, N. J. Zheng, U. Knipping, and I. S. T. Tsong,. Phys. Rev. B 38, 8444 (1988).

[8] A. Agarwal, T. E. Haynes, D. J. Eaglesham, H-J. Gossmann, D. C. Jacobson, J. M. Poate, and Y. E. Erokhin, Appl. Phys. Lett. **70**, 3332 (1997).

[9] J. P. Chang and H. H. Sawin, J. Vac. Sci. Technol. A **15**, 610 (1997).

[10] T. K. Chini, F. Okuyama, M. Tanemura, and K. Nordlund, Phys. Rev. B **67**, 205403 (2003).

[11] A. A. E. Stevens, W. M. M. Kessels, M. C. M. vande Sanden, and H. C. W. Beijerinck. J. Vac. Sci. Technol. A **24**, 1933 (2006).

[12] D. B. Graves and D. Humbird, Appl. Surf. Sci. **192**, 72 (2002).

[13] D. Humbird, D. B. Graves, A. A. E. Stevens, and W. M. M. Kessels, J. Vac. Sci. Technol. A **25**, 1529 (2007).

[14] T. Ohchi, S. Kobayashi, M. Fukasawa, K. Kugimiya, T. Kinoshita, T. Takizawa, S. Hamaguchi, Y. Kamide, and T. Tatsumi, Jpn. J. Appl. Phys. **47**, 5324 (2008).

[15] A. Matsuda, Y. Nakakubo, Y. Takao, K. Eriguchi, and K. Ono, Thin Solid Films **518**, 3481 (2010).

[16] C. Steinbrüchel, Appl. Phys. Lett. **55**, 1960 (1989).

[17] W. Eckstein, C. García-Rosales, J. Roth, and J. László, Nucl. Instrum. Methods Phys. Res. B **83**, 95 (1993).

[18] K. Ono, H. Ohta, and K. Eriguchi, Thin Solid Films **518**, 3461 (2010).

[19] Y. Osano and K. Ono, J. Vac. Sci. Technol. B **26**, 1425 (2008).

[20] P. Moroz, 52nd Annual Meeting of the APS Division of Plasma Physics, Nov. 2010, Bull. Am. Phys. Soc. Vol. 55, 15 (2010). Available at http://meetings.aps.org/Meeting/DPP10/Event/13219.

[21] T. Shimada, T. Yagisawa, and T. Makabe, Jpn. J. Appl. Phys. **45**, 8876 (2006).

[22] M. J. Kushner, J. Phys. D **94**, 194013 (2009).

[23] A. Sankaran and M. J. Kushner, J. Vac. Sci. Technol. A **22**, 1242 (2004).

[24] A. Sankaran and M. J. Kushner, J. Vac. Sci. Technol. A **22**, 1260 (2004).

[25] J. F. Ziegler, J. P. Biersack, and U. Littmark, *The Stopping and Range of Ions in Solids* (Pergamon, New York, 1985).

[26] E. H. Lee, G. R. Rao, and L. K. Mansur, Radiat. Phys. Chem. **55**, 293 (1999).

[27] D. Hegemann, H. Brunner, and C. Oehr, Nucl. Instrum. Methods Phys. Res. B **208**, 281 (2003).

[28] A. V. Vasenkov and M. J. Kushner, J. Appl. Phys. **95**, 834 (2004).

[29] K. P. Larsen, D. H. Petersen, and O. Hansen, J. Electrochem. Soc. **153**, G1051 (2006).

[30] P. Dixit and J. Miao, J. Phys.: Conf. Ser. **34**, 577 (2006).

[31] J. J. Végh, D. Humbird, and D. B. Graves, J. Vac. Sci. Technol. A **23**, 1598 (2005).